Sensitivity of compaction-induced multicomponent seismic time shifts to variations in reservoir properties

Steven Shawn Smith[1] and Ilya Tsvankin[1]

ABSTRACT

Pore-pressure variations inside producing reservoirs result in excess stress and strain that influence the arrival times of reflected waves. Inversion of seismic data for pressure changes requires better understanding of the dependence of compaction-induced time shifts on reservoir pressure reduction. Using geomechanical and full-waveform seismic modeling, we investigate pressure-dependent behavior of P-, S-, and PS-wave time shifts from reflectors located above and below a rectangular reservoir embedded in a homogeneous half-space. Our geomechanical modeling algorithm generates the excess stress/strain field and the stress-induced stiffness tensor as linear functions of reservoir pressure. Analysis of time shifts obtained from full-waveform synthetic data shows that they vary almost linearly with pressure for reflectors above the reservoir, but become nonlinear for reflections from the reservoir or deeper interfaces. Time-shift misfit curves computed with respect to noise-contaminated data from a reference reservoir for a wide range of pressure reductions display well-defined global minima corresponding to the actual pressure. In addition, we evaluate the influence of the reservoir width on time shifts and the possibility of constraining the width using time-lapse data. We also discuss the impact of moderate perturbations in the strain-sensitivity coefficients (i.e., third-order stiffnesses) on time shifts and on the accuracy of pressure inversion. Our feasibility analysis indicates that the most stable pressure estimation from noisy data is provided by multicomponent time shifts from reflectors below the reservoir. For multicompartment reservoirs, time shifts can be accurately modeled by linear superposition of the excess stress/strains computed for the individual compartments.

INTRODUCTION

Compaction-induced seismic traveltime shifts can potentially be inverted for pressure and fluid distributions inside a producing reservoir. Such an inversion contributes to the understanding of how fluids are moving (sweeping) through a reservoir, of levels of intercompartment pressure communication, and whether fluid is produced from locations away from the wells (Greaves and Fulp, 1987; Landrø, 2001; Lumley, 2001; Calvert, 2005; Hodgson et al., 2007; Wikel, 2008). Knowledge of reservoir pressure can also be used to estimate stress and strain variations outside the reservoir (Herwanger and Horne, 2005; Dusseault et al., 2007; Scott, 2007). Identifying those stress patterns helps to guide drilling decisions and reduce the cost of repairing or replacing wells snapped or sheared by high stresses.

Conventional methodologies employ poststack data and compaction-induced vertical stress/strain to estimate time-lapse velocity and volume changes (Hatchell and Bourne, 2005; Janssen et al., 2006; Carcione et al., 2007; Hodgson et al., 2007; Roste, 2007; Staples et al., 2007; De Gennaro et al., 2008). However, migration and stacking of data represents a complex filtering process that can corrupt phase relationships and arrival times. Further, velocity/strain estimation from field data using this approach often produces results that disagree with laboratory experiments (Bathija et al., 2009). Also, it has been shown that shear (deviatoric) strains generate significant time shifts, requiring the use of triaxial geomechanical interpretation of time-lapse data (Schutjens et al., 2004; Sayers and Schutjens, 2007; Herwanger, 2008; Sayers, 2010; Smith and Tsvankin, 2012). Finally, offset dependence of P-wave time shifts is sensitive to stress-induced anisotropy (Fuck et al., 2009).

Estimation of compaction-related time shifts requires geomechanical computation of excess strains, strain-induced stiffnesses, and modeling of time-lapse wavefields. Fuck et al. (2009, 2011)

develop a modeling methodology based on a triaxial strain formulation and the nonlinear theory of elasticity, and estimate P-wave shifts using anisotropic ray tracing. Smith and Tsvankin (2012) confirm the main results of Fuck et al. (2009) and analyze time shifts for S- and PS-waves using finite-difference elastic modeling. These studies demonstrate that volumetric (hydrostatic) and deviatoric (shear) strains generate significant time-shift contributions for all three (P, S, and PS) modes. According to the results of Smith and Tsvankin (2012), sensitivity of time shifts to reservoir pressure strongly varies with wave type and reflector location.

Here, we use geomechanical and finite-difference seismic modeling to study the dependence of P-, S-, and PS-wave time shifts on reservoir pressure. For a set of reflectors located above and below a single-compartment reservoir, we evaluate the linearity of time shifts expressed as a function of reservoir pressure. Time-shift misfits with respect to a reference reservoir are examined for a realistic range of pressure reductions and reservoir widths. We also study the sensitivity of pressure estimation to noise in the input data and to moderate errors in the third-order stiffness coefficients. We conclude by analyzing time shifts of P-, S-, and PS-waves for multicompartment reservoirs.

THEORETICAL BACKGROUND

Modeling traveltime shifts caused by production-induced changes in a reservoir is typically treated as a three-step process (Smith and Tsvankin, 2012). First, changes in reservoir parameters (here, pressure reduction) result in excess stress and strain in and around the reservoir (Figure 1). Second, the excess stress/strain perturbs the stiffness coefficients (C_{ij}) that govern the velocities and traveltimes of seismic waves. Third, the stress-induced stiffnesses are used to model time-lapse seismic data and compute the time shifts between the baseline and monitor surveys. In the tests below, we compute time shifts for the reflectors shown in Figure 2 for a
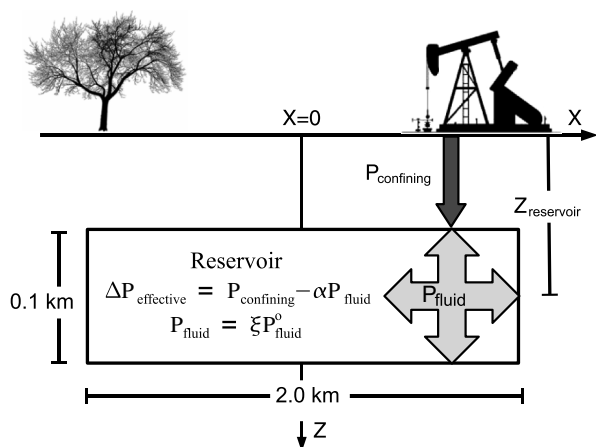

Figure 1. Reservoir geometry after Fuck et al. (2009) and Smith and Tsvankin (2012). Pore-pressure ($P_p = P_{fluid}$) reduction inside the reservoir results in an anisotropic velocity field due to the excess stress and strain. The reservoir is composed of and embedded in homogeneous Berea sandstone ($V_P = 2300$ m/s, $V_S = 1640$ m/s, $\rho = 2140$ kg/m³) with the following third-order stiffness coefficients: $C_{111} = -13,904$ GPa, $C_{112} = 533$ GPa, and $C_{155} = 481$ GPa (Sarkar et al., 2003). The effective stress coefficient α is introduced in equation 1. The coefficient ξ scales fluid pressure with respect to its initial value (see equation 1).

wide range of pressure reductions and corresponding changes in strain.

Strain, stiffness, and traveltime perturbation

We employ a simplified, 2D rectangular reservoir model after Fuck et al. (2009, 2011) (Figure 1), composed of isotropic Berea sandstone that follows standard Biot-Willis compaction theory (Hofmann et al., 2005; Zoback, 2007). The effective pressure in the reservoir (P_{eff}) changes according to a reduction in the pore fluid pressure (P_{fluid})

$$\Delta P_{eff} = P_c - \alpha P_{fluid} = P_c - \alpha(\xi P_{fluid}^0), \quad (1)$$

where $P_c = \rho gz$ is the confining pressure of the overburden, ρ is the density of the overburden column, g is acceleration due to gravity, z is reservoir depth, and α is known as the effective stress coefficient (Biot-Willis coefficient for "dry" rock, with air as the only pore infill; here, $\alpha = 0.85$). The coefficient ξ ($0 \leq \xi \leq 1$) expresses changes in the fluid pressure through its initial value, P_{fluid}^0, which corresponds to a stress/strain equilibrium. Velocities in the model are reduced by 10% from laboratory-measured values to account for differences between static and dynamic stiffnesses in low-porosity rocks (Yale and Jamieson, 1994). Pressure changes occur only inside the reservoir block.

By definition,

$$\alpha = 1 - \frac{K_a}{K_g}, \quad (2)$$

where K_a is the aggregate bulk modulus of the material, and K_g is the bulk modulus of the grains (Zoback, 2007). The value of K_a varies with pore volume and the pressure-dependent bulk moduli of the pore fluid and matrix (Batzle and Han, 2009; Fjær, 2009). As the material compacts and fluid is removed, the aggregate bulk modulus of the rock approaches that of the grains ($K_a \rightarrow K_g$), and α tends to zero (Hornby, 1996). For the range of pressure/strain changes used in our studies, we assume uniform fluid type ("dead oil"), such that fluid moduli and K_a remain constant. Also, depressurization of the reservoir compartment is taken to be uniform. Finally, the material is assumed to remain undamaged and to behave in a linear fashion. Therefore, the value of α in our algorithm stays constant. However, for cases where compaction-induced changes in the rock are sufficiently large, α will vary with pressure, porosity, or bulk moduli. This will make effective pressure changes in equation 1 nonlinear in P_{fluid}.

The resulting displacement, stress, and strain changes throughout the section can be computed from analytic equations discussed by Hu (1989), Downs and Faux (1995), and Davies (2003). However, here we perform geomechanical modeling using the finite-element, plane-strain solver from COMSOL (COMSOL AB, 2008), which has the ability to handle more complicated, multicompartment reservoir geometries. Based on the reduction in the effective pressure, COMSOL computes displacement changes and changes to stress and strain as linear functions of ΔP_{eff} and, in our algorithm, of the fluid pressure P_{fluid}. The 2.0 km × 0.1 km reservoir is located in a 20 km × 10 km model space to obtain stress, strain, and displacement close to those for a half-space. Here, we model a single-compartment 2D reservoir, assuming that the reservoir length in the X_2-direction is large. Reducing the out-of-plane reservoir

dimensions or adding 3D structure may perturb the in-plane stress/strain field, requiring the use of a 3D geomechanical model. Further, pressure variations inside the reservoir or segmentation of the reservoir volume by faults will require a multicompartment geomechanical model (an example is discussed below).

Typical modeled volumetric and deviatoric strains for the range of pressures used in our study are shown in Figure 3 for reflector A (Figure 2) and for a horizontal line through the center of the reservoir. The volumetric strain (a scalar), which is equal to one-third of the trace of the strain tensor, varies linearly with reservoir pressure, as expected (Figure 3a). The components of the deviatoric strain tensor have been summed to illustrate that its variation with pressure reduction is also linear (Figure 3b). The modeled strains in Figure 3 are one or two orders of magnitude higher inside the reservoir than in the overburden, and are comparable to those given by Barton (2006) for compacting reservoirs.

The strain-induced variations of the stiffness tensor c_{ijkl} can be expressed using the so-called nonlinear theory of elasticity (Hearmon, 1953; Thurston and Brugger, 1964; Fuck et al., 2009)

$$c_{ijkl} = c_{ijkl}^0 + \frac{\partial c_{ijkl}}{\partial e_{mn}} \Delta e_{mn}$$
$$= c_{ijkl}^0 + c_{ijklmn} \Delta e_{mn}, \qquad (3)$$

where c_{ijkl}^0 is the second-rank stiffness tensor of the background (unperturbed) medium, c_{ijklmn} is a sixth-order tensor containing the derivatives of the second-order stiffnesses with respect to strain, and Δe_{mn} is the excess strain tensor. Despite the term "nonlinear," which applies to Hooke's law, equation 3 expresses the stiffnesses c_{ijkl} as linear functions of the strains Δe_{mn}. Thus, because the strains Δe_{mn} in equation 3 are linear functions of the pressure reduction ΔP_{eff}, so are the second-order stiffnesses c_{ijkl}.

Wave propagation through the stressed medium is modeled using Hooke's law with the stiffness tensor c_{ijkl}. By applying the Voigt convention, the tensor c_{ijklmn} can be converted into a matrix $C_{\alpha\beta\gamma}$, as described by Fuck and Tsvankin (2009). For 2D models, we need only two elements of that matrix (C_{111} and C_{112}), and employ the values measured on Berea sandstone samples by Sarkar et al. (2003) (Figure 1). It should be noted that measurements of C_{111} and C_{112} are rare, and both coefficients are estimated with significant uncertainty. For actual reservoir conditions, the coefficients $C_{\alpha\beta\gamma}$ can vary with pressure, temperature, and saturation. Such in situ changes are particularly important should α tend toward zero, as this would compound variations of the stiffnesses c_{ijkl} that determine velocity. Here, however, we hold the coefficients C_{111} and C_{112} constant, which keeps the stiffnesses c_{ijkl} linear functions of Δe_{mn} and reservoir pressure.

While we work with full-waveform data generated by finite differences, the influence of local stiffness perturbations on time shifts can be easier understood by analyzing traveltimes computed along rays. Fuck et al. (2011) obtain the P-wave time shifts δt along a certain raypath using a Fermat integral with the integrand linearized in the excess strains:
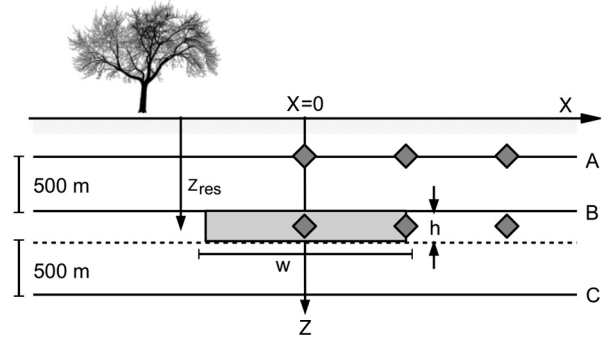

Figure 2. Reservoir (shaded) and reflectors (marked A, B, and C) used in our study. Strains in Figure 3 are measured at $X = 0$ km, 1 and 2 km on reflector A and on a horizontal line through the reservoir center (marked by gray diamonds).
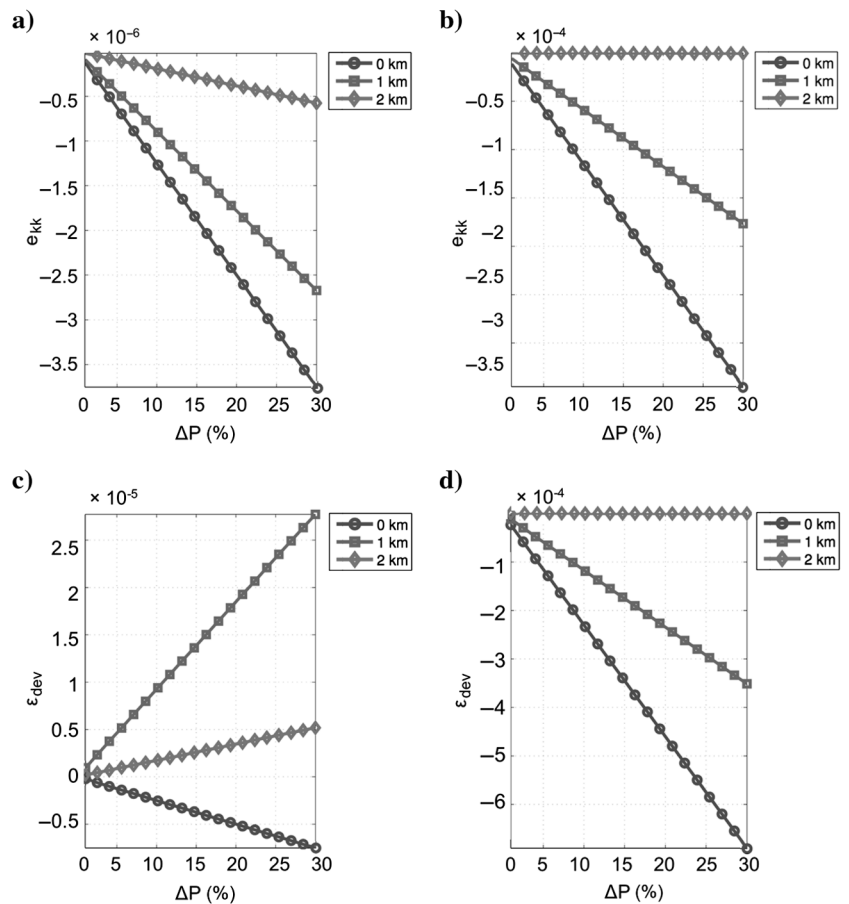

Figure 3. Strains generated by geomechanical modeling of a reservoir at 1.5 km depth (Figure 1). (a, b) Volumetric and (c, d) deviatoric strains at (a, c) reflector A and (b, d) on a horizontal line through the center of the reservoir. Legends on each plot indicate horizontal distances from the reservoir center (see diamond markers in Figure 2). In this and the following figures, ΔP is the percentage change in reservoir fluid pressure, which can be expressed through the coefficient ξ in equation 1 as $\Delta P = (1 - \xi)100$.

$$\delta t = \frac{1}{2} \int_{\tau_1}^{\tau_2} [B_1 \, \Delta e_{kk} + B_2 \, (\mathbf{n}^T \Delta \boldsymbol{\epsilon} \, \mathbf{n})] \, d\tau, \qquad (4)$$

where Δe_{kk} is the change of the volumetric strain (e_{kk} is 1/3 of the trace of strain tensor), $\Delta \boldsymbol{\epsilon}$ is the change of the deviatoric strain tensor, $\mathbf{n}$ is the slowness vector, and

$$B_1 = \frac{C_{111} + 2C_{112}}{3C_{33}^0}, \qquad B_2 = \frac{C_{111} - C_{112}}{C_{33}^0}, \qquad (5)$$

where C_{33}^0 is the background stiffness coefficient. Equation 4 is valid only for small stiffness perturbations. The first term of the integrand in equation 4 corresponds to time shifts due to volumetric (hydrostatic) strains, while the second term accounts for the contribution of deviatoric (shearing) strains. Clearly, the time shifts described by equation 4 are linear in excess strains and, therefore, in the pressure drop inside the reservoir.

In general, however, time shifts are nonlinear in the stiffness coefficients. Indeed, even the P-wave velocity in a homogeneous, isotropic medium is given by $\sqrt{C_{33}/\rho}$, and the traveltime over distance R is

$$t = R \sqrt{\frac{\rho}{C_{33}}} \, . \qquad (6)$$

From equations 4 and 6, we expect time shifts to vary linearly only for small changes in stiffness (ΔC_{ij}). Therefore, it is important to evaluate the range of pressure drops, and thus Δe_{mn} and ΔC_{ij}, for which traveltime shifts can be accurately described as linear functions of stiffnesses and reservoir pressure. Additional nonlinearity could be introduced by a pressure/porosity-dependent effective stress coefficient α (equations 1 and 2) or variations in the coefficients $C_{\alpha\beta\gamma}$, but such variations are not accounted for by our modeling algorithm.

The character of the pressure dependence of time shifts from specific reflectors influences the methodology one would use to invert for reservoir pressure. Should time shifts vary linearly with reservoir pressure, estimation of the pressure drop ΔP is possible with standard linear inversion techniques. Otherwise, it is necessary to employ a nonlinear/global inversion method.

Time-shift trends versus reflector depth

Smith and Tsvankin (2012) use an elastic finite-difference algorithm to model P-, S-, and PS-wave reflections for baseline ($P_{\text{fluid}} = P_{\text{fluid}}^0$) and monitor surveys. Time shifts for each wave type are computed by isolating specific arrivals in the baseline and monitor surveys, computing trace-by-trace crosscorrelations between the surveys, and smoothing the resulting time-shift curves. Figure 4 shows typical time-shift surfaces (hulls) for a reservoir at 1.5 km depth with a pressure drop of 20%, constructed using data from 22 reflectors located between the surface and $z = 3$ km. For P-waves (Figure 4a), the results are close to those obtained by ray tracing (Fuck et al., 2009). Strain-induced P-wave velocity anisotropy around the reservoir causes offset-dependent traveltime shifts. Laterally varying P-wave time-shift patterns below the reservoir are due to elevated shearing (deviatoric) strains at the reservoir endcaps. The excess strain does not cause substantial SV-wave anisotropy because the resulting symmetry of the medium is close to elliptical.

Time shifts for various wave types/reflector combinations exhibit different sensitivities to reservoir pressure changes. For P-waves above and below the reservoir, time shifts vary with offset due to changing deviatoric stress around the reservoir (Figure 4a). The combination of increased volumetric and deviatoric strains inside the reservoir generates large S- and PS-wave time shifts from reflectors beneath it (Figure 4b and 4c). These trends provide useful guidance for designing a stable pressure-inversion procedure. For this study, reflectors A, B, and C (Figure 2) are used to measure time shifts of P-, S- and PS-waves for a range of pressure drops and to evaluate the linearity of the pressure dependence of time shifts.

P-wave time shifts in Figure 4 are somewhat larger than typical values measured in the field (Guilbot and Smith, 2002; Hatchell and Bourne, 2005; Herwanger et al., 2007; Hodgson et al., 2007; Rickett et al., 2007; Staples et al., 2007; De Gennaro et al., 2008). Smaller values of the third-order stiffnesses $C_{\alpha\beta\gamma}$, or a decrease in the effective stress coefficient (α) at larger pressure drops will reduce the magnitude of modeled time shifts. However, direct comparison of our results with time shifts from real-world reservoirs is nontrivial. In particular, we use laboratory data for rock samples with an R-factor that is much higher than that estimated from field data (Hatchell and Bourne, 2005; Bathija et al.,
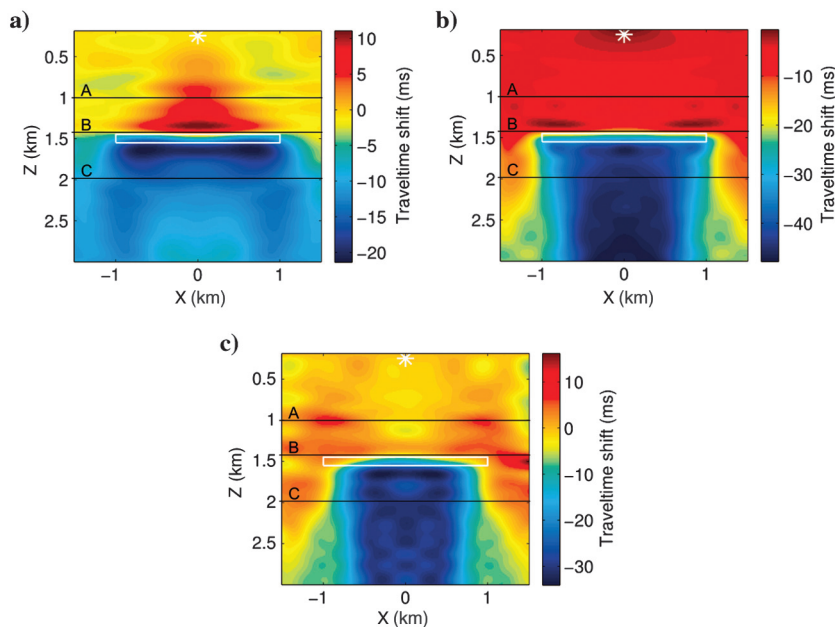

Figure 4. Typical time-shift surfaces for (a) P-waves, (b) S-waves, and (c) PS-waves, measured using 22 reflectors around the reservoir of Figure 1 (Smith and Tsvankin, 2012). The time shifts correspond to hypothetical specular reflection points at each (X, Z) location in the subsurface. Positive shifts indicate lags and negative shifts are leads. Source location is indicated by the white asterisk on top; $\Delta P = 20\%$. Reflectors A, B, and C from Figure 2 are shown for reference.

2009). Also, third-order stiffnesses obtained in a laboratory may not be suitable for modeling reservoirs without certain adjustment.

Complex reservoir models typically incorporate multiple updates (history matching) of geology and rock-physics properties (strain, velocity, porosity, saturation, temperature, and R-factor) using well-log data (Staples et al., 2007; De Gennaro et al., 2008). Although this approach cannot be implemented here, the spatial patterns in Figure 4 will remain largely unchanged by rock-property updates. For example, the spatial distribution of P-wave time shifts in Figure 4a is similar to that of the time shifts from the Stillwater field shown by Staples et al. (2007), despite differences in time-shift magnitudes.

METHODOLOGY

Modeling and assumptions

Here, we examine the variation of compaction-induced time shifts for the three reflectors from Figure 2 due to the pressure drop and the corresponding stiffness change $\Delta C_{ij}(x, z)$. The initially homogeneous stiffness/velocity field across the section becomes heterogeneous and anisotropic as reservoir pressure is reduced. Following geomechanical finite-element modeling of compaction-induced strain [$\Delta e_{mn}(x, z)$], changes in the stiffnesses are computed from equation 3. These stiffnesses are used by an elastic finite-difference code (Sava et al., 2010) to generate shot records of reflected waves.

Reflectors A, B, and C are inserted as density perturbations to sample traveltimes and estimate time shifts for each shot. Then, the multi-component synthetic data are processed to isolate arrivals from the specific reflector, and time shifts between the reference (baseline) and monitor reservoir models are computed by crosscorrelation. P-wave time shifts are measured from the shot records of the vertical displacement, while S- and PS-shifts are measured on the horizontal component. Additional smoothing is applied to reduce time-shift anomalies caused by interfering arrivals that distort the wavelet shape. For all models discussed here, the reservoir depth is 1.5 km, and the source is located above the center of the reservoir ($X = 0$).

Misfit (objective) functions

In the tests below, we individually vary reservoir pressure and width. Misfits (objective functions) between P-, S-, and PS-wave's time shifts for a given reservoir (Δt) and reference reservoir model (Δt^{ref}) are computed as the L2-norm,

$$\mu = \sqrt{\sum_{k=1}^{N} (\Delta t_k^{\text{ref}} - \Delta t_k)^2}, \tag{7}$$

where $k = 1, 2, \ldots, N$ are the individual traces in the shot record. The time-shift misfit between a modeled (test) reservoir and the reference reservoir is calculated by depressurizing both reservoirs from the zero-stress/strain initial state. Joint misfit is found as the L2-norm of the individual wave type misfits,

$$\mu_{\text{joint}} = \sqrt{\mu_P^2 + \mu_S^2 + \mu_{PS}^2}. \tag{8}$$

Misfits discussed below have not been normalized to facilitate comparison of results for different wave types at specific reflectors.

Computing joint misfits (equation 8) allows one to gauge the possible advantages of combining different data types in pressure estimation. When analyzing field data, geologic structures and interference from out-of-plane events may limit the effective length of reflecting interfaces. Similarly, strong amplitude variations with offset may occur due to fluid movement or partial depletion of the reservoir (i.e., compartmentalization). In these cases, combining time shifts from multiple reflectors and wave types may be desirable or even necessary. Further, it is possible to assign weights to wave types (equation 8) or individual reflectors depending on the data quality (i.e., the number and signal-to-noise ratio of arrivals).

ANALYSIS

Time shifts and sensitivity to reservoir pressure

Figure 5 shows measured time shifts of P-, S- and PS-waves reflected from interfaces A, B, and C for a set of 20 reservoir pressure drops of up to 30% of the initial reservoir fluid pressure. Positive shifts indicate lags where monitor survey reflections arrive later than those in the baseline survey, and negative shifts are leads. Data for S- and PS-waves do not include time-shift estimates at $X = 0$ due to the low amplitudes of the horizontal displacement from a vertical force at small offsets. These time-shift curves are shown as-is, without smoothing. Artifacts in these curves are time-measurement errors due to distortions in the monitor wavelet caused by interfering arrivals (see Smith and Tsvankin, 2012)

In general, P-wave time-shift lags at reflector A (top row) are linear with pressure drop, and are associated with a P-wave velocity reduction above the reservoir. S-waves reflected from interface A experience small velocity increases and time-shift leads due to changes in the stiffness C_{55} in the overburden. At small source-receiver offsets, PS-wave shifts above the reservoir are close to zero because P-lags are almost canceled by S-leads (Smith and Tsvankin, 2012). At reflector B, time shifts for all three modes exhibit slightly nonlinear behavior with increasing pressure drop. Time shifts from reflector C are clearly nonlinear as a function of pressure because of the large stiffness perturbations inside the reservoir.

Therefore, if the data have a sufficiently high signal-to-noise ratio, time shifts for reflectors above the reservoir can be inverted using standard linear inverse methods. Reflections from beneath the reservoir produce quasi-linear time shifts for a small pressure drop, but they become nonlinear in pressure after 10–20% depressurization. Accordingly, time shifts of P-, S-, and PS-waves reflected from deep interfaces should be processed by a nonlinear inversion algorithm.

As a second aspect of our feasibility study, we evaluate the sensitivity to pressure of total time shifts at all offsets for specific modes and reflectors. For this discussion, the term "higher sensitivity" indicates a combination of high time-shift values and a steeply sloped misfit curve with a distinct minimum at the reference (true) pressure value (Figure 6c, for example). L2-norm time-shift misfits (equation 7) for 20 pressure drops of up to 30% were computed with respect to the reference reservoir in Figure 1, having a pressure drop of 15% [halfway between 10% and 20% pressure drops shown in Smith and Tsvankin (2012), and approximately equal to the 5 MPa pressure drop of Fuck et al. (2009)].

The results for P-, S-, PS-waves along with joint misfits (equation 8) are shown in Figure 6. Misfit curves correlate well with the time-shift magnitudes for each wave type and reflector depth

in Figures 2 and 4, and the global minima coincide with the actual 15% pressure drop. For reflector A, PS-wave time shifts at larger offsets provide greater sensitivity to lower pressure drops than do time shifts of P- and S-waves. At the top of the reservoir (reflector B), P-wave time shifts change most rapidly with pressure deviation from the reference value. The magnitudes of cumulative P-wave shifts through the overburden are largest at reflector B, and extend along the entire top reservoir boundary (see Figure 4a). S-wave shifts clearly provide the largest sensitivity for all pressure drops beneath the reservoir (reflector C). However, in all cases, the joint misfit is more sensitive to pressure than the misfit for any single wave type.

Sensitivity to errors in C_{111} and C_{112}

As previously mentioned, there are only a few available measurements of the third-order stiffness coefficients needed to compute strain-induced changes in the second-order stiffnesses (equation 3). The published values of C_{111} and C_{112} may also contain significant uncertainty as they were not obtained under in situ stress and

saturation conditions. Therefore, it is important to evaluate the sensitivity of the modeled time shifts and pressure estimation to variation in C_{111} and C_{112} (see equation 5).

Figure 7 shows L2-norm time-shift misfits obtained in the same way as those in Figure 6, but with distorted values of C_{111} and C_{112}. The coefficients C_{111} and C_{112} of the reference reservoir remain fixed at the values from Figure 1. The misfits in Figure 7 are computed for S-waves from reflector B, but are indicative of the general behavior of all wave types at all reflectors. Changing C_{111} by ±20% causes substantial variations in the time shifts; in particular, a higher magnitude of C_{111} results in larger stiffness perturbations (Figure 7a). The sensitivity of the time shifts to C_{112} is much lower because that coefficient is smaller than C_{111}. All combined permutations of distorted values of C_{111} and C_{112} (Figure 7b) cause some deviations from the unperturbed L2-misfit curves, mostly due to errors in C_{111}. According to equation 3, strain-related stiffnesses are proportional to the product of $C_{\alpha\beta\gamma}$ and the pressure drop ΔP. Therefore, 20% perturbations in C_{111} cause an approximately 20% displacement of the minimum of the misfit curve along the
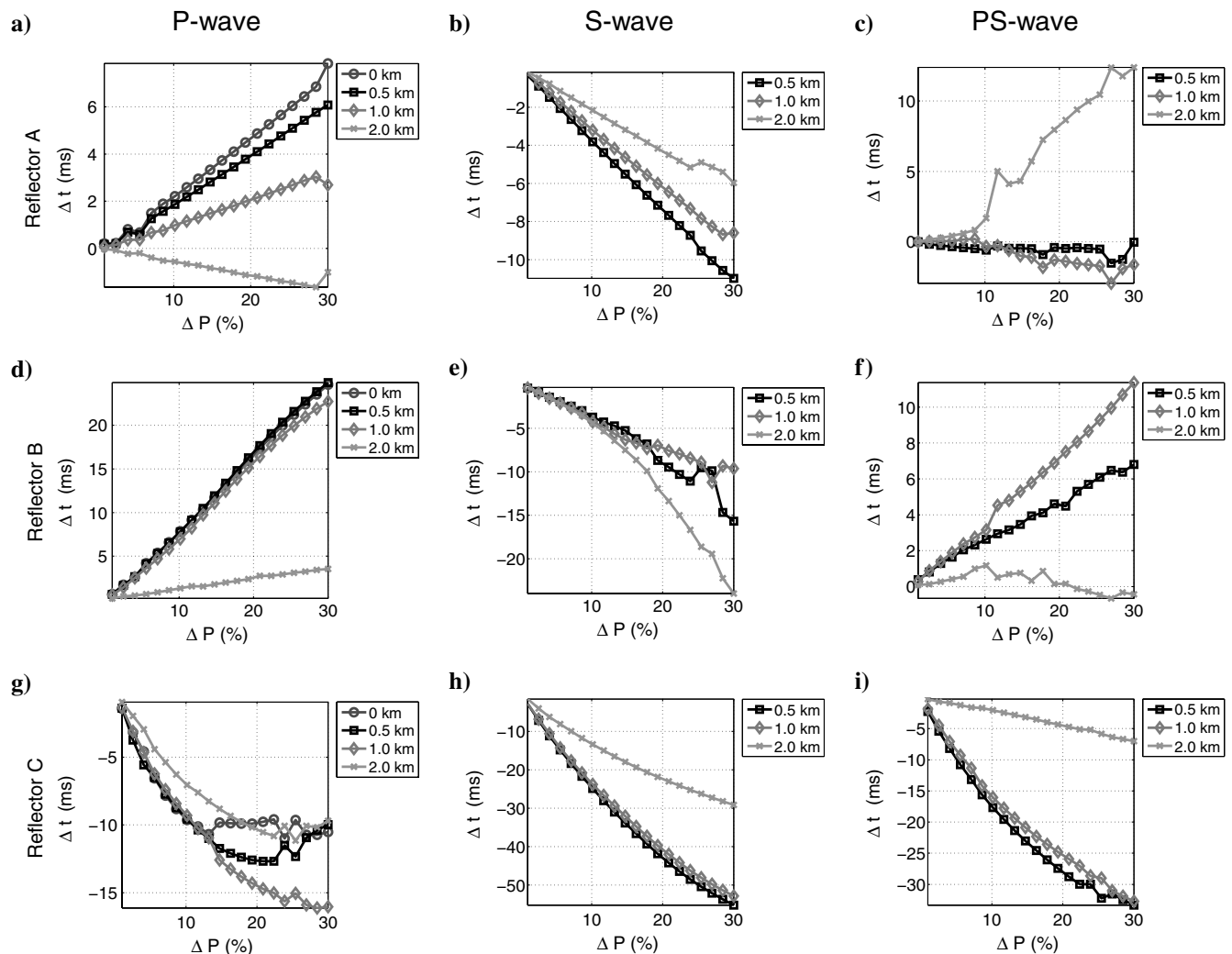

Figure 5. Time shifts for reservoirs with pressure drops up to 30%. The source is located above the center of the reservoir at $X = 0$. (a, b, c) reflector A, (d, e, f) reflector B, and (g, h, i) reflector C. Columns correspond to (a, d, g) P-wave, (b, e, h) S-wave, and (c, f, i) PS-wave. Plot legends indicate receiver X-coordinate.

pressure axis (i.e., a 20% increase in C_{111} is compensated by a 20% decrease in ΔP).

Influence of reservoir width

Whereas reservoir depth is typically well known from borehole data, the true width of the reservoir (or a given reservoir compartment) may be estimated with an error. Because the stress/strain field around the reservoir is a function of the compartment dimensions, the strain-dependent time shifts change with reservoir width. In particular, shear (deviatoric) stresses are largest at the endcaps of the reservoir, even for reservoirs of elliptical shape (Smith and Tsvankin, 2012). The distance between these shear-strain anomalies varies with reservoir width, thus changing the ratio of volumetric to deviatoric strain around the reservoir. An illustration of this variation for multicompartment reservoirs is shown in Figure 11g and 11h below.

Figure 8 displays time shifts of P-, S- and PS-waves at reflectors A, B, and C for reservoir width ranging from 0.5 to 4 km. The reference reservoir width for misfit measurements is 2 km. Time shifts above reflector A do not vary significantly with reservoir width, except when shearing strains from the reservoir endcaps are close to one another. However, directly above the reservoir at reflector B, P-wave time shifts change by up to 10 ms. The largest time shifts occur for smaller source-receiver offsets at reflector C for wider (exceeding 3 km) reservoirs with $\Delta P = 15\%$, reaching magnitudes similar to those for the reservoir with $\Delta P = 20\%$ shown in Figure 4. The elevated time shifts in the region below the center of wider reservoirs (at reflector C) are indicative of a more significant compaction within the reservoir (i.e., the ratio of the vertical-to-horizontal strain inside the reservoir increases with reservoir width). The sensitivity curves for P-, S-, and PS-waves (Figure 9) are reasonably smooth, with the exception of the S-wave misfit for reflector B and a reservoir width of 3 km (this is likely due to a processing artifact). As is the case with pressure dependence, joint misfit data from reflector C are most sensitive to variations in reservoir width.

We have also studied the influence of distortions in the stiffnesses C_{111} and C_{112} on the time-shift misfits computed as functions of reservoir width. As discussed above, the magnitude of time shifts changes significantly for $\pm 20\%$ variation in C_{111} (less so for variations in C_{112}), which results in perturbations for the misfits of all wave types at reflector C (similar to those of the ΔP misfit minima in Figure 7). In particular, the largest shift of the misfit minimum at reflector C occurs for S-waves, producing a $\pm 10\%$ deviation from the reference value (2 km). Little deviation of the misfit minimum for 20% perturbations to C_{111} and C_{112} occurs at reflectors A and B. An exception is the misfit curve for S-waves at reflector A, where the C_{111} perturbation shifts the misfit minimums by up to 50% of the reference width. This is due to compaction-induced lateral variations of the stiffness C_{55} in the overburden (i.e., between the reservoir and the surface). Similar misfit deviations do not occur for P-waves at reflector A because significant spatial variations of stiffness C_{33} take place primarily inside the reservoir (Smith and Tsvankin, 2012).
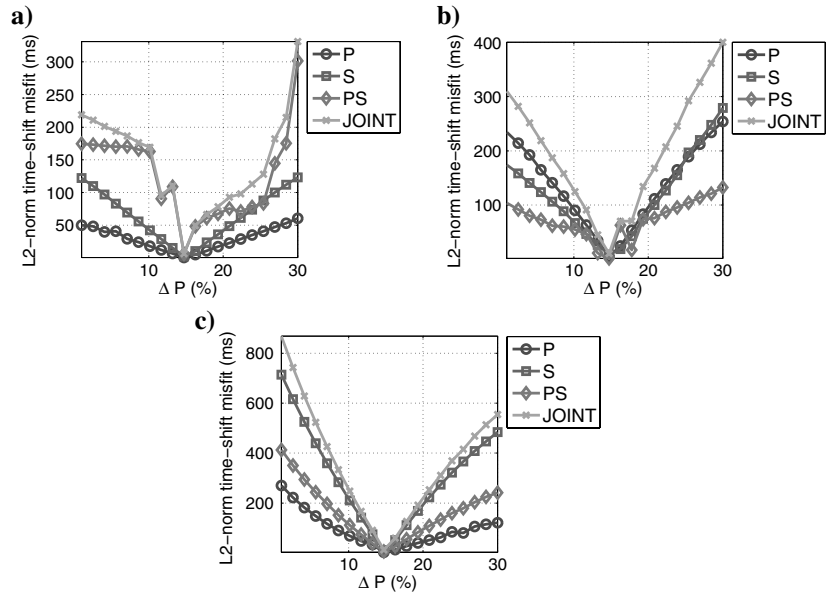

Figure 6. L2-norm misfits of time shifts for reservoir pressure drops ranging from 0% to 30%. The reference reservoir corresponds to a pressure drop of 15%. (a) Reflector A, (b) reflector B, and (c) reflector C.
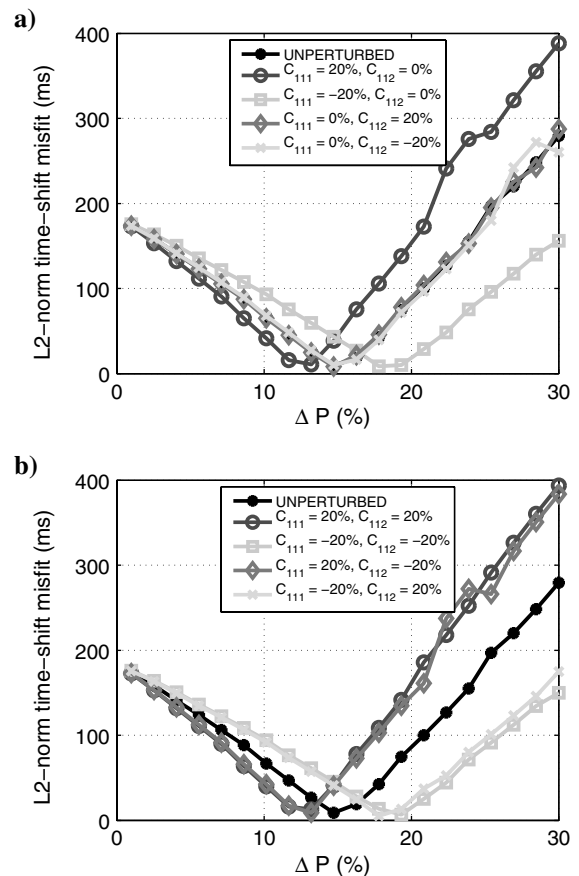

Figure 7. L2-norm misfits of time shifts for S-waves from reflector B computed with distorted third-order stiffness coefficients C_{111} and C_{112}. The values of C_{111} and C_{112} for the reference reservoir (at $\Delta P = 15\%$) are unchanged. The coefficients C_{111} and C_{112} are distorted by $\pm 20\%$ (a) independently; (b) simultaneously.
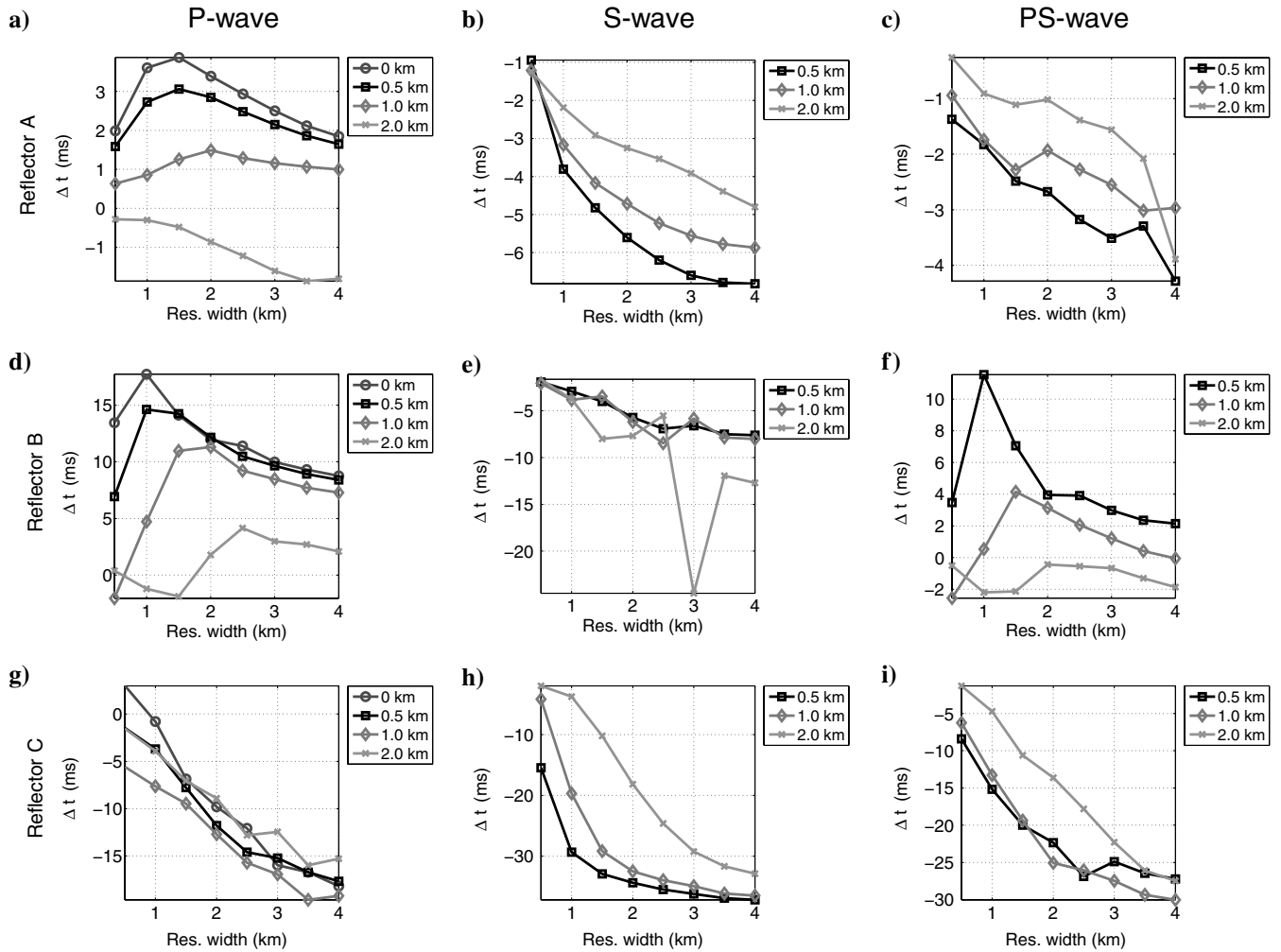
Figure 8. Time shifts for reservoir width ranging from 0.5 to 4 km. Pressure drops for all reservoirs are 15%. (a, b, c) Reflector A, (d, e, f) reflector B, and (g, h, i) reflector C. (a, d, g) P-wave, (b, e, h) S-wave, and (c, f, i) PS-wave. Plot legends indicate receiver X-coordinate.

Figure 9. L2-norm misfits of time shifts for reservoir width ranging from 0.5 to 4 km computed with respect to a 2 km-wide reference reservoir (Figure 1). The pressure drop for all models is 15%. (a) Reflector A, (b) reflector B, and (c) reflector C (see Figure 2).
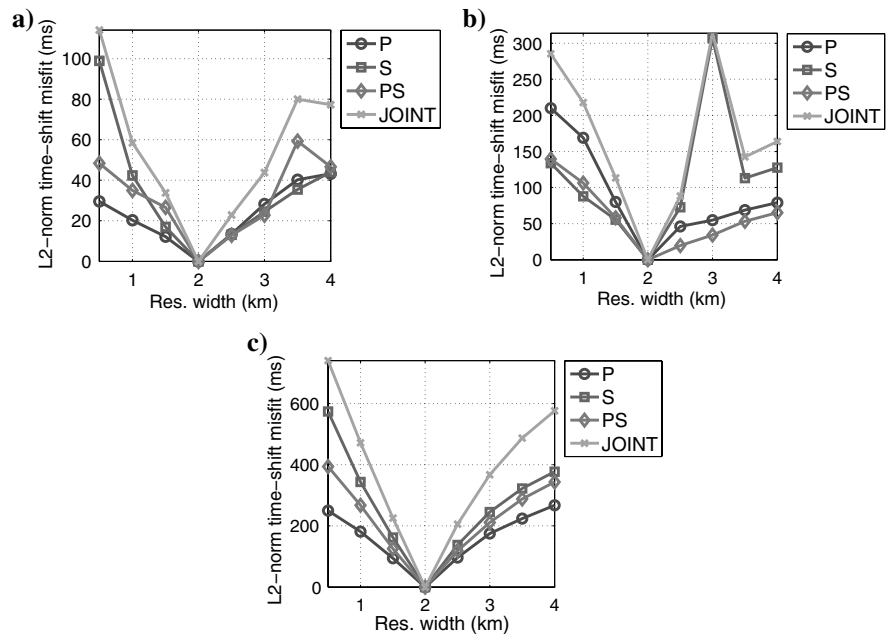
Sensitivity to noise in reference time shifts

The influence of Gaussian noise with standard deviations of 2, 5, and 10 ms added to the time shifts for the reference reservoir (Figures 5 and 6) is shown in Figure 10. The largest noise level is chosen to be sufficient to obfuscate typical P-wave time-shift values, but not so high as to be unrealistic. Time-shift misfits for 2-ms noise (left column) do not differ significantly from the corresponding noise-free estimates in Figure 6. Substantial degradation in sensitivity is observed for reflectors A and B for 5-ms noise (Figure 10b and 10e). The misfit curves develop local minima, indicating that a linear inversion algorithm may fail at moderate noise levels. For stronger noise reaching 10 ms (approximately 2/3 of the maximum P-wave time shifts for noise-free data), the misfit curves for reflectors A and B are significantly distorted. Time shifts of all wave types for reflector C, however, are sufficiently large to still provide smooth sensitivity curves with a clear global minimum and minimal degradation. Predictably, as noise levels increase, the sensitivity to pressure reduction declines, but joint sensitivity for reflectors B and C remains reasonably high. Hence, in the presence of substantial noise, joint and S-wave time shifts for reflectors

below the reservoir provide the most reliable input data for pressure inversion.

Strain fields for multicompartment reservoirs

Next, we examine the possibility of modeling strain fields for multicompartment reservoirs by linear superpositions of strains generated by each compartment. Inversion of time-shift data for pressure variations in multicompartment reservoirs can help evaluate the pressure distribution away from the wellbore.

Following the description of subsurface displacement by Segall (1992) as an integral of a pressure-dependent Green's function, Hodgson et al. (2007) invert for pressure in multicompartment reservoirs. They express the vertical strain at a point (x, z) outside the reservoir as the sum of the pressure changes (equation 1) in the individual compartments multiplied by a Green's function that depends on the compartment stiffness, shape, and depth (Mindlin and Cheng, 1950; Sen, 1951).

We have shown that time shifts for triaxial stress/strain geomechanical models are approximately linear in reservoir pressure as long as the pressure drop and, thus, the corresponding stiffness
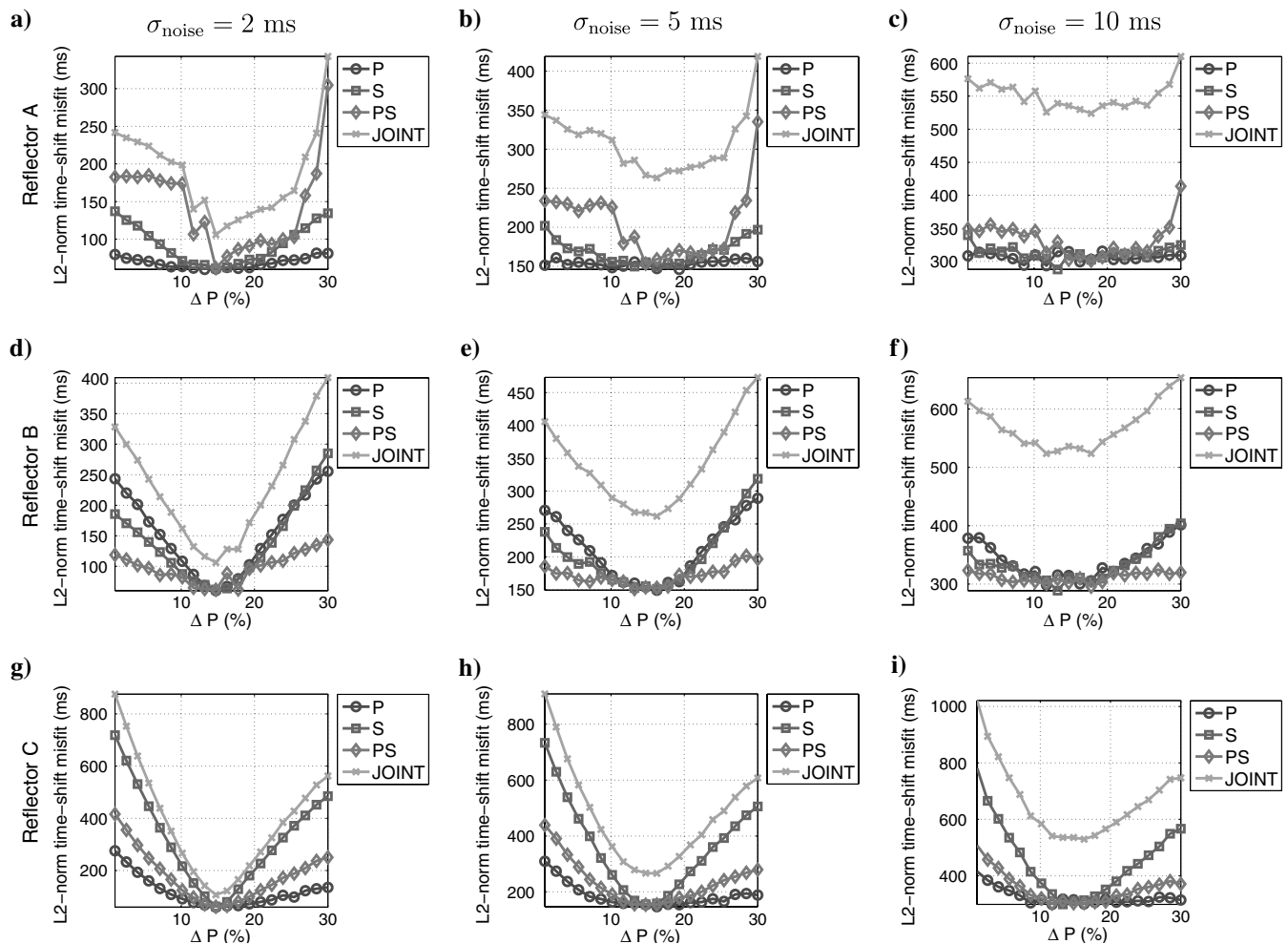

Figure 10. L2-norm misfits for noise-contaminated reference time shifts as a function of reservoir pressure drop (compare with the corresponding noise-free misfits in Figure 6). The reference reservoir pressure drop is 15%. (a, b, c) Reflector A, (d, e, f) reflector B, and (g, h, i) reflector C. The standard deviation of noise increases by column: (a, d, g) ±2 ms, (b, e, h) ±5 ms, and (c, f, i) ±10 ms.

changes are small. Here, we verify the superposition principle of Hodgson et al. (2007) for multicompartment geomechanical models. The strain field of a reservoir compartment is a function of its size and properties (i.e., of the compartment Green's function). The addition of other compartments alters the background medium around the first compartment and, therefore, changes that compartment's strain field. Thus, even for small pressure reductions, the strain field (and the resulting stiffnesses and time shifts) of a multicompartment reservoir may somewhat differ from the sum of the contributions of each compartment. This is a manifestation of "crosstalk," where the presence of other compartments influences the response of any single compartment computed in isolation.

We compare time shifts for the single compartment, 2 km-wide reservoir of Figure 1 to those for a 2-km wide reservoir composed of two 1 km-wide subcompartments centered at $X = \pm 0.5$ km. The pressure drop in each compartment is 20%. Time shifts for the second multicompartment reservoir are computed by the linear superposition of the strain fields of the smaller, 1-km wide compartments. First, the strain fields are computed for a single, 1 km-wide reservoir (Figure 11a, 11d, and 11g). To obtain the strains for a second, 1 km-wide reservoir symmetric with respect to $X = 0$, these strain fields are mirrored across the $X = 0$ axis. We then add the strain fields for both reservoirs (Figure 11b, 11e, and 11h) and use them in the time-shift modeling process prior to computing the stiffness coefficients. While the strains $e_{11}(+x, z)$ and $e_{33}(+x, z)$ are symmetric with

respect to the same elements at $x < 0$, it is necessary to reverse the sign of $e_{13}(+x, z)$ to find $e_{13}(-x, z)$.

The strain-field patterns in Figure 11 for the single compartment, 1 km-wide (a, d, g), and 2 km-wide (c, f, i) reservoirs are quite similar. There are slight differences in the "projection" of the element e_{33} into the surrounding medium attributable to differences in reservoir width (also see Fuck et al., 2011).

The time shifts of P-, S-, and PS-waves for all three reservoirs from Figure 11 are shown in Figure 12. The 1 km-wide reservoir centered at $X = 0.5$ km (Figure 12a, 12b, and 12c) exhibits time-shift asymmetry and lensing effects discussed in Smith and Tsvankin (2012). The spatially varying time shifts for the 2 km-wide reservoir composed of two subcompartments (Figure 12d, 12e, and 12f) and those for the single-compartment reservoir (Figure 12g, 12h, and 12i) are almost identical. Small oscillatory differences between the S-wave time shifts are due to polynomial fitting/smoothing employed in postprocessing (Smith and Tsvankin, 2012). Similar oscillations occur in the PS-wave time shifts above the two-compartment reservoir (Figure 12f), but the PS-wave shifts beneath the reservoir are similar for both cases.

Although it is not feasible to perform this comparison for a wide range of reservoir models, these results indicate that time shifts obtained by linear superposition of the strain fields of multiple compartments are close to the time shifts of a compound, single-compartment reservoir. This assumes that the strains are
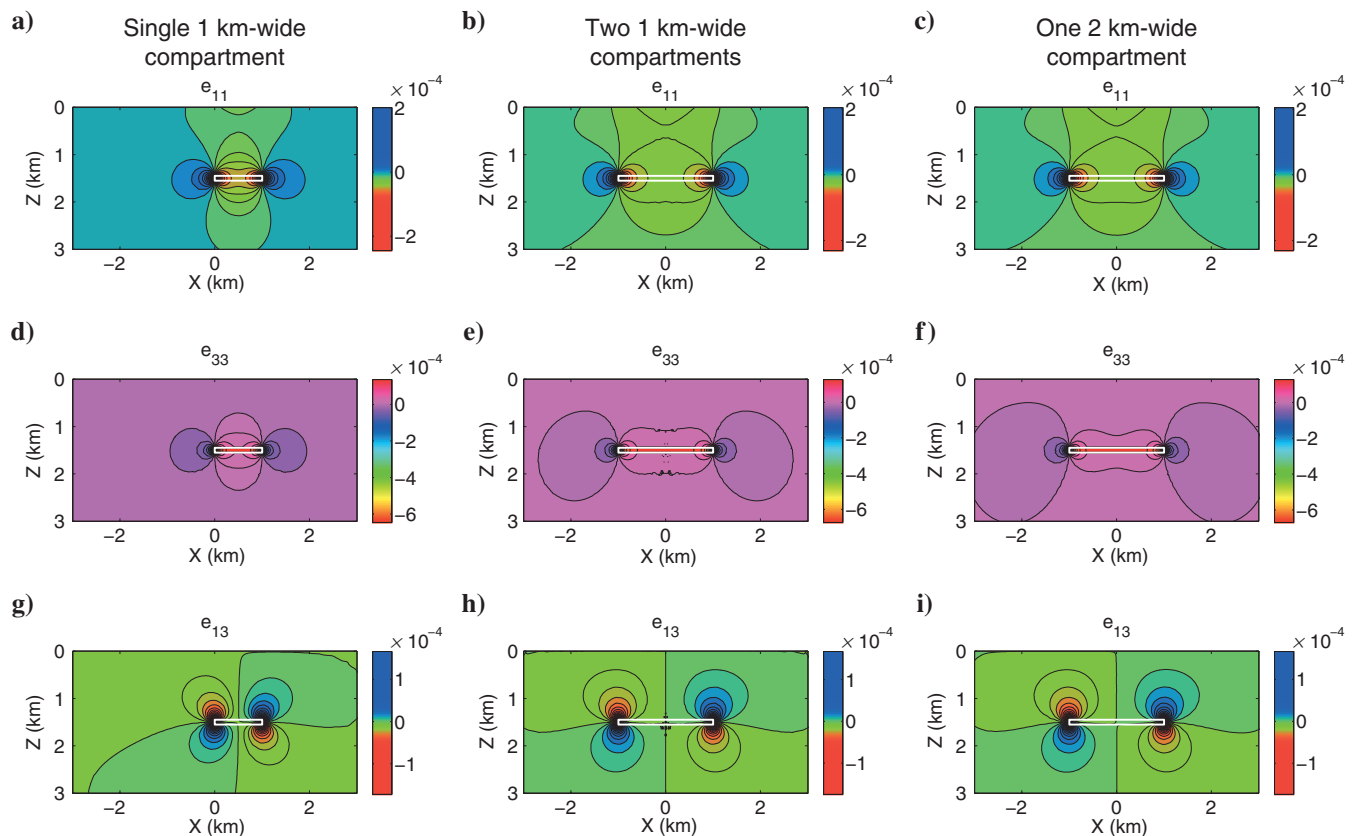

Figure 11. Comparison of strains computed for a reservoir constructed from two subcompartments (b, e, h) 1 km-wide (a, d, g show the strains for one subcompartment) and a single compartment 2 km-wide (c, f, i). (a, b, c) Horizontal strain, (d, e, f) vertical strain, and (g, h, i) shear strain. The pressure drop is 20%.
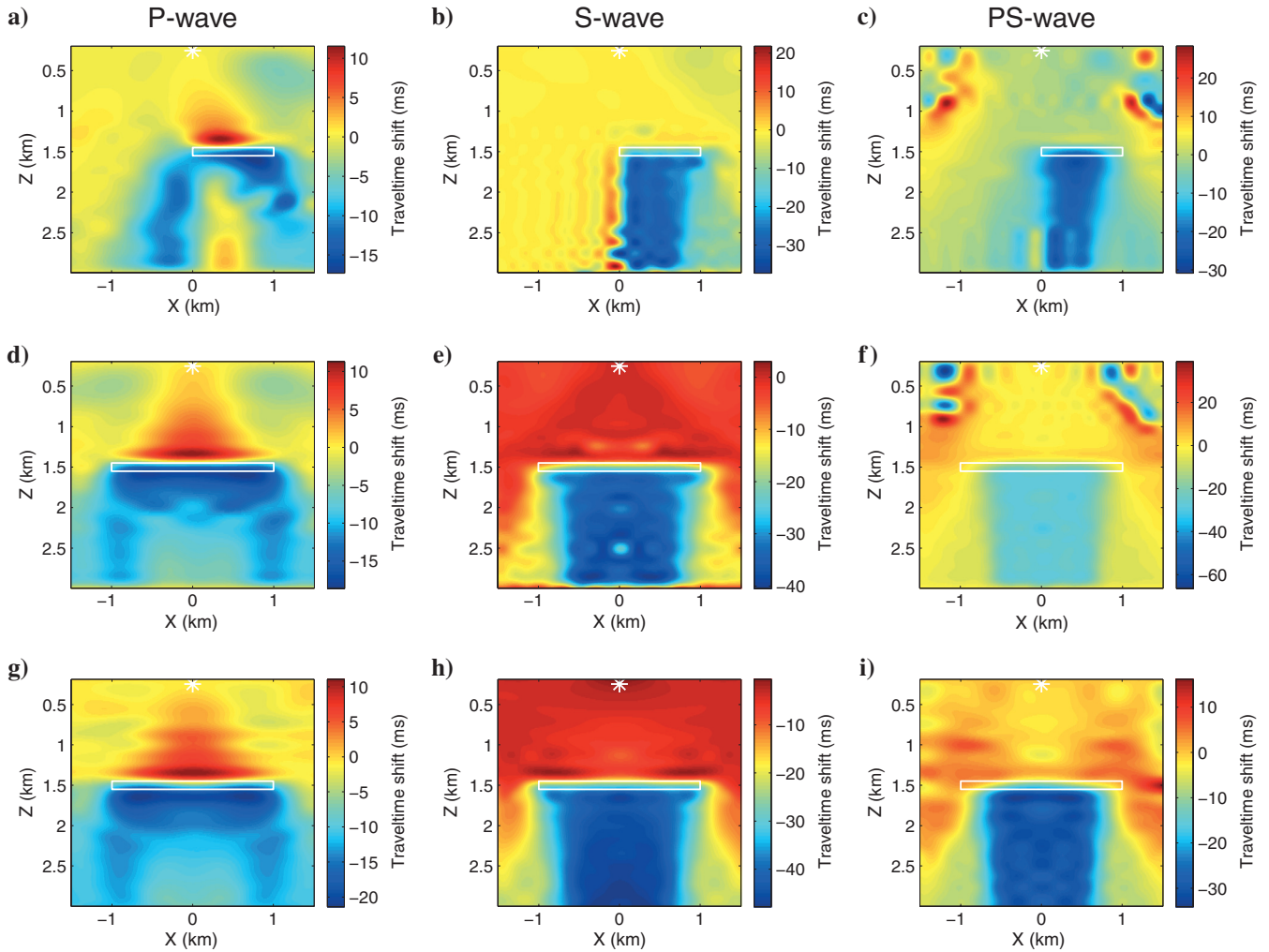
Figure 12. P-, S-, and PS-wave time shifts for a reservoir constructed from two subcompartments 1 km-wide (a, b, c show time shifts for one subcompartment) to form a reservoir 2 km-wide (d, e, f). Time shifts for a single-compartment reservoir 2 km-wide (g, h, i) are shown for comparison. Pressure drop for all compartments/reservoirs is 20%. (a, d, g) P-wave, (b, e, h) S-wave, and (c, f, i) PS-wave. Plots (d, e, f) are generated by adding the strain fields of both subcompartments prior to computing stiffnesses.

sufficiently small, because superposition of large strains from multiple subcompartments becomes inadequate due to the differences between the corresponding Green's functions (Mindlin and Cheng, 1950).

CONCLUSIONS

We have studied the dependence of P-, S- and PS-wave time shifts on reservoir pressure with the goal of assessing the feasibility of pressure and width estimation for a 2D rectangular reservoir. The model comprises a homogeneous block of Berea sandstone, where pore-pressure changes inside the reservoir induce heterogeneous stress/strain and stiffness fields throughout the medium. Geomechanical modeling is implemented with a finite-element solver that generates excess stress and strain as a linear function of reservoir pressure. Multicomponent seismic data are modeled by an elastic finite-difference code, and resulting time shifts are computed by specialized postprocessing. Whereas the stress-induced stiffness

tensor is linear in excess strain, traveltime shifts generally depend on the stiffness coefficients in a nonlinear fashion.

In the regions with relatively small strain, pressure-related perturbations in the stiffnesses are not sufficiently large to cause nonlinearity of time shifts. For example, time shifts are linear in pressure reduction for reflectors above the reservoir. However, strains inside the reservoir are much larger than those in the surrounding medium, creating large stiffness changes. Thus, waves reflected from points inside and below the reservoir generally exhibit nonlinear time-shift dependence on pressure.

L2-norm misfits of time shifts computed with respect to a reference reservoir show that S-wave reflections from interfaces beneath the reservoir provide the most sensitive data for pressure estimation. Misfit curves for S-wave shifts from deep reflectors have well-defined global minima at the correct pressure value even for reference time shifts contaminated with 10-ms noise. This suggests that inversion for reservoir pressure with noisy data should operate with (preferably multicomponent) reflections from beneath the reservoir.

One source of uncertainty in interpretation of time-lapse data is the strain-sensitivity tensor (i.e., third-order stiffnesses), which is poorly constrained by existing measurements. Although time shifts vary substantially with the coefficient C_{111} (the other coefficient, C_{112}, is much smaller in our model), errors of up to 20% in the third-order stiffnesses do not alter the general shape of the time-shift misfit curves. Still, the minimum misfit moves from the correct pressure value, with the percentage deviation close to the error in C_{111}.

Rock-property differences between laboratory and in situ (i.e., from seismic or borehole data) measurements are illustrated by large discrepancies between lab- and field-estimated R-factors. It may be possible to scale velocities measured on small, dry, low-temperature samples in the lab to in situ velocity values. When applied to reservoir models of the type used here, this may yield modeled time shifts that are closer to those estimated from field data.

Another important parameter that can be potentially estimated from time shifts is the width of the reservoir. The magnitude of time shifts increases with reservoir width in a nonlinear fashion. Our sensitivity analysis indicates that, as with pressure estimation, the most reliable information for constraining reservoir width is provided by deep S-wave reflections.

Our numerical testing confirms that time shifts for multicompartment reservoirs can be modeled by superposition of the strain fields generated by the individual compartments. Such linear superposition, however, is valid only when the excess stress/strain is sufficiently small. Superposition of the strain-induced time shifts computed for each subcompartment is much less accurate because time shifts are nonlinear in strain and stiffness.

For reservoirs composed of a single or multiple compartments, a linear inversion method may be sufficient for pressure estimation as long as pressure changes are small (up to approximately 10%). However, time shifts measured at larger pressure drops should be inverted by a more general, nonlinear (global) algorithm.

ACKNOWLEDGMENTS

REFERENCES

Barton, N., 2006, Rock quality, seismic velocity, attenuation and anisotropy: Taylor & Francis.

Bathija, A. P., M. Batzle, and M. Prasad, 2009, An experimental study of the dilation factor: Geophysics, **74**, no. 4, E181–E191, doi: 10.1190/1.3137060.

Batzle, M., and D. Han, 2009, Rock and fluid properties: Seismic rock physics: SEG Continuing Education Series, Denver Geophysical Society.

Calvert, R., 2005, Insights and methods for 4D reservoir monitoring and characterization: Distinguished instructor short course: SEG.

Carcione, J. M., M. Landrø, A. F. Gangi, and F. Cavallini, 2007, Determining the dilation factor in 4D monitoring of compacting reservoirs by rock-physics models: Geophysical Prospecting, **55**, 793–804, doi: 10.1111/j.1365-2478.2007.00633.x.

COMSOL AB, 2008, COMSOL multiphysics. COMSOL AB, http://www.comsol.com/.

Davies, J. H., 2003, Elastic field in a semi-infinite solid due to thermal expansion of a coherently misfitting inclusion: Journal of Applied Mechanics and Technical Physics, **70**, 655–660, doi: 10.1115/1.1602481.

De Gennaro, S., A. Onaisi, A. Grandi, L. Ben-Brahim, and V. Neillo, 2008, 4D reservoir geomechanics: A case study from the HP/HT reservoirs of the Elgin and Franklin fields: First Break, **26**, 53–59.

Downs, J., and D. A. Faux, 1995, Calculation of strain distributions in multiple-quantum-well strained-layer structures: Journal of Applied Physics, **77**, 2444–2447, doi: 10.1063/1.358771.

Dusseault, M. B., S. Yin, L. Rothenburg, and H. Han, 2007, Seismic monitoring and geomechanics simulation: The Leading Edge, **26**, 610–620, doi: 10.1190/1.2737119.

Fjær, E., 2009, Static and dynamic moduli of a weak sandstone: Geophysics, **74**, no. 2, WA103–WA112, doi: 10.1190/1.3052113.

Fuck, R. F., A. Bakulin, and I. Tsvankin, 2009, Theory of traveltime shifts around compacting reservoirs: 3D solutions for heterogeneous anisotropic media: Geophysics, **74**, no. 1, D25–D36, doi: 10.1190/1.3033215.

Fuck, R. F., and I. Tsvankin, 2009, Analysis of the symmetry of a stressed medium using nonlinear elasticity: Geophysics, **74**, no. 5, WB79–WB87, doi: 10.1190/1.3157251.

Fuck, R. F., I. Tsvankin, and A. Bakulin, 2011, Influence of background heterogeneity on traveltime shifts for compacting reservoirs: Geophysical Prospecting, **59**, 78–89, doi: 10.1111/j.1365-2478.2010.00909.x.

Greaves, R. J., and T. J. Fulp, 1987, Three-dimensional seismic monitoring of an enhanced oil recovery process: Geophysics, **52**, 1175–1187, doi: 10.1190/1.1442381.

Guilbot, J., and B. Smith, 2002, 4-D constrained depth conversion for reservoir compaction estimation: Application to Ekofisk Field: The Leading Edge, **21**, 302–308, doi: 10.1190/1.1463782.

Hatchell, P., and S. Bourne, 2005, Rocks under strain: Strain-induced time-lapse time shifts are observed for depleting reservoirs: The Leading Edge, **24**, 1222–1225, doi: 10.1190/1.2149624.

Hearmon, R., 1953, 'Third-order' elastic coefficients: Acta Crystallographia, **6**, 331–340, doi: 10.1107/S0365110X53000909.

Herwanger, J., 2008, R we there yet?: 70th Annual International Meeting, EAGE, Extended Abstracts.

Herwanger, J., and S. Horne, 2005, Predicting time-lapse stress effects in seismic data: The Leading Edge, **24**, 1234–1242, doi: 10.1190/1.2149632.

Herwanger, J., E. Palmer, and C. R. Schiøtt, 2007, Anisotropic velocity changes in seismic time-lapse data: 77th Annual International Meeting, SEG, Expanded Abstracts, **26**, 2883–2887.

Hodgson, N., C. MacBeth, L. Duranti, J. Rickett, and K. Nihei, 2007, Inverting for reservoir pressure change using time-lapse time strain: Application to Genesis Field, Gulf of Mexico: The Leading Edge, **26**, 649–652, doi: 10.1190/1.2737104.

Hofmann, R., X. Xu, M. Batzle, M. Prasad, A.-K. Furre, and A. Pillitteri, 2005, Effective pressure or what is the effect of pressure?: The Leading Edge, **24**, 1256–1260, doi: 10.1190/1.2149644.

Hornby, B. E., 1996, Experimental investigation of effective stress principles for sedimentary rocks: 66th Annual International Meeting, SEG, Expanded Abstracts, 1707–1710.

Hu, S. M., 1989, Stress from a parallelepipedic thermal inclusion in a semispace: Journal of Applied Physics, **66**, 2741–2743, doi: 10.1063/1.344194.

Janssen, A. L., B. A. Smith, and G. W. Byerley, 2006, Measuring velocity sensitivity to production-induced strain at the Ekofisk field using time-lapse time-shifts and compaction logs: 76th Annual International Meeting, SEG, Expanded Abstracts, 3200–3204.

Landrø, M., 2001, Discrimination between pressure and fluid saturation changes from time lapse data: Geophysics, **66**, 836–844, doi: 10.1190/1.1444973.

Lumley, D., 2001, Time-lapse seismic reservoir monitoring: Geophysics, **66**, 50–53, doi: 10.1190/1.1444921.

Mindlin, R. D., and D. H. Cheng, 1950, Nuclei of strain in the semi-infinite solid: Journal of Applied Physics, **21**, 926–930, doi: 10.1063/1.1699785.

Rickett, J., L. Duranti, T. Hudson, B. Regel, and N. Hodgson, 2007, 4D time strain and the seismic signature of geomechanical compaction at Genesis: The Leading Edge, **26**, 644–647, doi: 10.1190/1.2737103.

Roste, T., 2007, Monitoring overburden and reservoir changes from prestack time-lapse seismic data — applications to chalk fields: Ph.D. thesis, Norwegian University of Science and Technology.

Sarkar, D., A. Bakulin, and R. L. Kranz, 2003, Anisotropic inversion of seismic data for stressed media: Theory and a physical modeling study on Berea sandstone: Geophysics, **68**, 690–704, doi: 10.1190/1.1567240.

Sava, P., J. Yan, and J. Godwin, 2010, SFEWE elastic finite difference wave-propagation development code for the Madagascar seismic software collection: http://www.reproducability.org.

Sayers, C. M., 2010, Geophysics under stress: Geomechanical applications of seismic and borehole acoustic waves: Distinguished instructor short course: SEG.

Sayers, C. M., and P. M. Schutjens, 2007, An introduction to reservoir geomechanics: The Leading Edge, **26**, 597–601, doi: 10.1190/1.2737100.

Schutjens, P. M. T. M., T. H. Hanssen, M. H. H. Hettema, J. Merour, P. de Bree, J. W. A. Coremans, and G. Helliesen, 2004, Compaction-induced porosity/permeability reduction in sandstone reservoirs: Data and model for elasticity-dominated deformation: SPE Reservoir Evaluation & Engineering, SPE 88441, 202–216.

Scott, T. E., 2007, The effects of stress path on acoustic velocities and 4D seismic imaging: The Leading Edge, **26**, 602–608, doi: 10.1190/1.2737101.

Segall, P., 1992, Induced stresses due to fluid extraction from axisymmetric reservoirs: Pure and Applied Geophysics, **139**, no. 3/4, 535–560, doi: 10.1007/BF00879950.

Sen, B., 1951, Note on the stresses produced by thermoelastic strain in a semi-infinite elastic solid: Quarterly of Applied Mathematics, **8**, 365–369.

Smith, S., and I. Tsvankin, 2012, Modeling and analysis of compaction-induced traveltime shifts for multicomponent seismic data: Geophysics, **77**, no. 6, T221–T237, doi: 10.1190/geo2011-0332.1.

Staples, R., J. Ita, R. Burrel, and R. Nash, 2007, Monitoring pressure depletion and improving geomechanical models of the Shearwater field using 4D seismic: The Leading Edge, **26**, 636–642, doi: 10.1190/1.2737120.

Thurston, R. N., and K. Brugger, 1964, Third-order elastic constants and the velocity of small amplitude elastic waves in homogeneously stressed media: Physical Review, **133**, A1604–A1610, doi: 10.1103/PhysRev.133.A1604.

Wikel, K. R., 2008, Three-dimensional geomechanical modeling of a tight gas reservoir, Rulison Field, Colorado: M.Sc. thesis, Colorado School of Mines.

Yale, D. P., and W. H. Jamieson, 1994, Static and dynamic mechanical properties of carbonates, *in* P. P. Nelson, and S. E. Laubach, eds., Rock mechanics, models, and measurements challenges from industry: Proceedings of the 1st North American Rock Mechanics Symposium, 463–471.

Zoback, M. D., 2007, Reservoir geomechanics: Cambridge University Press.